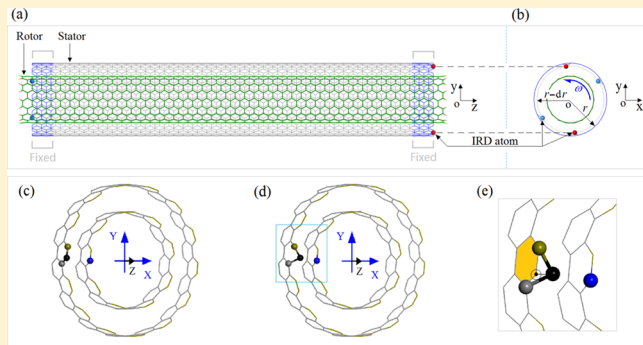


Spectrum of Temperature-Dependent Rotational Frequency of the Rotor in a Thermally Driven Rotary Nanomotor

Kun Cai,^{*†‡} Jingzhou Yu,[†] Jiao Shi,[†] and Qing H. Qin^{*‡§ID}[†]College of Water Resources and Architectural Engineering, Northwest A&F University, Yangling 712100, China[‡]Research School of Engineering, The Australian National University, Canberra, ACT 2601, Australia**S Supporting Information**

ABSTRACT: By fixing of the outer tube of double-walled carbon nanotubes, a thermally driven rotary nanomotor can be obtained one or more carbon atoms at the end of the stator have an obvious inward radial deviation. Due to the asymmetry of the potential field of the stator, a collision between two tubes leads to the axial component of angular momentum that drives the rotation of the rotor. Relative sliding between the two tubes is resisted due to the roughness of the potential field of stators. Hence, the rotational frequency of the rotor has a maximal value in the balanced state. The spectrum of rotational frequency with respect to temperatures from 8 to 2000 K is presented by means of molecular dynamics simulation. The temperature interval is divided into five zones on the basis of the characteristics of the spectrum. In the robust zone, the nanomotor exhibits stationary rotation. In the controllable zone, the rotational frequency of rotor can be adjusted by varying the temperature. In particular, if a rotating rotor is cooled to an ultralow temperature, the final stable value of the rotational frequency is still very high and is slightly lower than the maximal value rather than zero; i.e., the nanomotor will theoretically never stop rotating.



1. INTRODUCTION

In 2016, the Nobel Prize in Chemistry was awarded to three researchers for their contributions to the development of nanomachines.¹ This award inspired researchers to undertake both experimental and theoretical study of the development of relevant nanodevices. A nanomotor, a kind of nanodevice that transfers chemical or external field energy into motion, is an essential part of a nanomachine. Practically, an ideal nanomachine should have at least the following five features: it is simply fabricated, easily controlled, has strong robustness in ambient conditions, has sufficient output power, and is multifunctional. Most existing nanomachines, however, have only some of these features.^{2–6} Hence, fundamental research into nanomotors requires still more input from researchers to achieve a desired nanomachine.

Carbon nanotubes (CNTs), discovered in 1991,⁷ have become popular in recent years as low-dimensional materials.^{8–11} Due to their high in-shell modulus and ductility^{12–15} and ultralow intershell friction,^{16–19} multiwalled/double-walled carbon nanotubes (M/DWNTs) are desirable candidates for fabricating nanodevices such as nano-oscillators,^{20–23} nanobearings,^{24–26} nanostrain sensors,^{27–29} linear nanomotors,^{30,31} and rotary nanomotors.^{32–36} For example, Fennimore et al. developed a rotary nanomotor using MWNTs as the shaft in an electronanomotor. The rotation of a rotor formed from several blades attached to the MWNT shaft was driven by the external electric field. Theoretical models of nanomotors driven by an

external electric field have been developed by other researchers, e.g., Tu and Hu³³ and Wang et al.³⁴ Using mimicking, Kang and Hwang³⁵ proposed a theoretical model for a nanomotor driven by nanofluid. Hamdi et al.³⁶ presented a nanomotor in which electrostatic attraction could induce rotation of inner tubes in two axially aligned MWNTs with opposite chirality.

Unlike the aforementioned models of rotary nanomotors from CNTs, a thermally driven rotary nanomotor (Figure 1) constructed from DWNTs was introduced in 2014.^{37,38} In those investigations, the outer tube was partly or wholly fixed (acting as a stator) after the system had fully relaxed under a canonical (*NVT*) ensemble (with *N* the number of atoms, *V* the volume, and *T* the temperature). The rotation of the rotor was excited after a certain period of relaxation. Meanwhile, both the magnitude and directional sense (“sense” here means forward/backward or upward/downward application of a force or other physical field) of rotation of the rotor were unpredictable. A breakthrough occurred at the end of 2015, when it was found that the sense of rotation of the inner tube (rotor) under a canonical ensemble with a constant temperature could be controlled by specifying inward radial deviation (IRD) of a carbon atom at a fixed end of the outer tube (stator).³⁹ Cai et al. suggested some methods for observing and

Received: May 16, 2017**Revised:** June 27, 2017**Published:** July 14, 2017

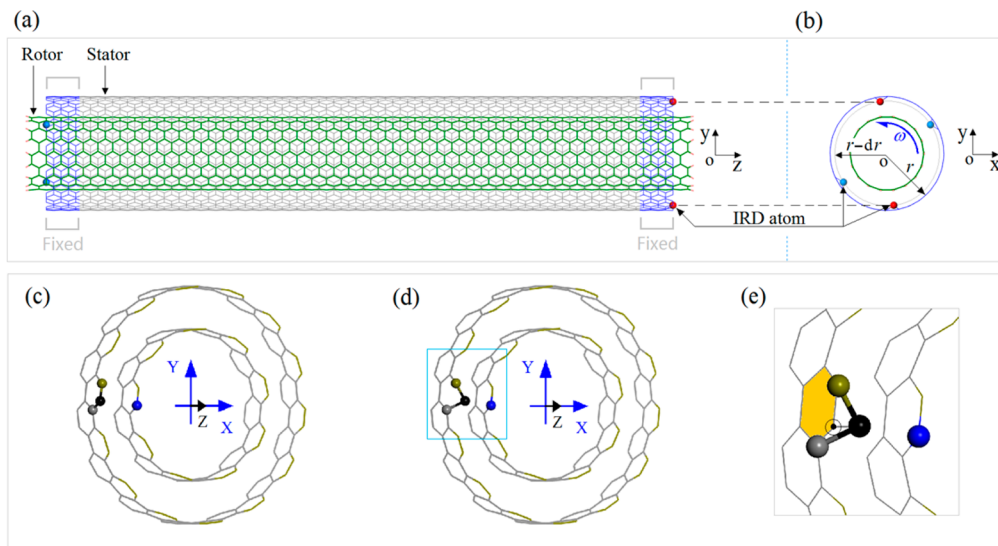


Figure 1. Schematic geometry of a thermally driven rotary nanomotor made from (9,9)/(14,14) DWNTs. The lengths of the rotor (inner tube) and stator (outer tube) are 11.07 and 10.45 nm, respectively. The ends of the rotor are hydrogenated. At each end of the stator (outer tube) are two atoms with the same IRD of $dr = 0.3l_{c-c}$, i.e., pink IRD atoms at the left end and red IRD atoms at the right end. $l_{c-c} = 0.142$ nm. The atoms in the blue area on the stator are fixed during simulation. ω is the rotational speed of the rotor in gigahertz (GHz). (c–e) IRD of the black atom at the end of the stator: (c) the black atom has no IRD; (d) only the black atom has IRD; (e) amplified local configuration in (d). The black atom has dislocated from its original position (a corner of the green honeycomb).

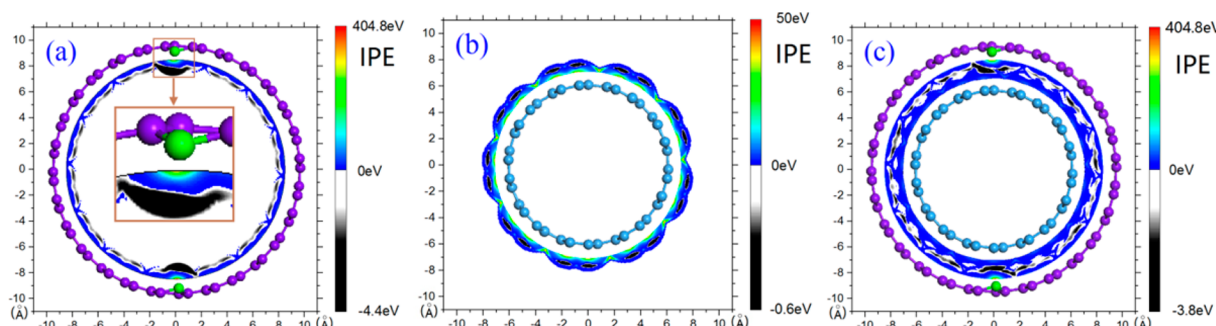


Figure 2. IPE fields within the cross section of the initial tubes in Figure 1. An IPE field is generated by scanning the cross section that passes through the atoms with IRD on the (14,14) stator with a carbon atom. The minimum distance between the scanning atom and the normal atoms on the tubes is set at 1 Å (0.1 nm). The IPE is obtained using the total potential energy in the current system plus the scanning atom, minus the potential energy of isolated tube(s). (a) IPE field within the (14,14) tube with two atoms with IRD. The field is asymmetric. (b) IPE field outside the (9,9) rotor, being symmetric. (c) IPE field between the rotor and stator on the cross section that crosses atoms with IRD. This field is also asymmetric. Due to the inward radial deviation of the green atoms on the stator, the IPE value near an atom with IRD varies from negative (between white and black in the contour plots) to positive (between blue and red in the contour plots) in (a) or (c). Near an IRD atom, the maximum gradient of the IPE exists between the maximum and minimum IPE. 0-IPE refers to the isoline of the IPE with respect to 0 eV, which is the white-blue interface in the field.

even measuring the rotation of the rotor.^{40,41} Then recently, Yang et al.⁴² tested the output power of a thermally driven rotary nanomotor. But the temperature range involved in the studies was usually only within [100, 500] K. In fact, from ultralow to ultrahigh temperatures, energy transmission among the atoms on DWNTs occurs quite differently. Typically, intertube friction can be neglected at ultralow temperatures but it becomes significant for stable rotation of the rotor at high temperatures. This feature has limited the application of such ensembles. This work presents a study of the performance of a nanomotor over a wider temperature range. First, we discuss the mechanism of the directional rotation of the rotor by means of theoretical analysis. Then, the spectrum of the output rotational frequency of the rotor is obtained by scanning temperatures from 8 to 2000 K. The wide range of temperatures considered should benefit understanding of the

mechanism of directional rotation of nanomotors. Finally, we place the nanomotor in a canonical ensemble with varying temperature to simulate its dynamic behavior in the practical environment.

2. MODEL AND METHODS

2.1. Model. In the nanomotor shown in Figure 1, both the magnitude and the direction of the atoms' velocity would clearly be different from those of the system in a Nosé–Hoover thermostat.⁴³ The magnitude and direction of the velocities with respect to thermal vibration obey Gaussian distribution. When the temperature is relatively high, the thermal vibration of the atoms is so dramatic that the collision between rotor and stator can drive an obvious motion of the rotor. In particular, when some atoms on the stator have an obvious IRD, they collide with the rotor more frequently than any other atom on

the stator. In **Figure 2**, the interaction potential energy (IPE) fields near the tube(s) in the nanomotor (**Figure 1**) are illustrated. We can see that the IPE near an atom with IRD (**Figure 2a**) is not distributed as symmetrically as that near the rotor (**Figure 2b**). Moreover, both the maximum (red) and the minimum (black) of the IPE appear in a location very close to the IRD atom. This configuration indicates that the maximal gradient of the field is between the maximum and minimum points so that a slight displacement in this area would produce a significant change in potential energy. Hence, atoms near an atom with IRD are first attracted and then very strongly repelled so that collisions between atoms with IRD and the rotor occur more easily than with other atoms on the stator. At the same time, the maximum of the potential energy is 2 orders of magnitude greater than its minimum. Hence, thermal vibration of atoms on the rotor is easily induced by the strong repulsion from an atom with IRD. The IPE field between two tubes (**Figure 2c**) is also asymmetric. Moreover, we find that the 0-IPE isolines (IPE isoline with respect to 0 eV) (white-blue interfaces in **Figure 2**)⁴⁴ are not connected and not smooth. Hence, any relative sliding between two tubes must overcome potential barriers because the intertube friction resists the rotation of the rotor.

The asymmetry of the IPE fields near the two atoms with IRD indicates that a collision provides a nonzero component of angular momentum⁴⁵ about the tube axis that drives a unidirectional rotation of the rotor. Supposing that the collision provides angular momentum on the rotor about a tube axis (*z*-axis), e.g., H1, the rotation of the rotor is accelerated when the collision occurs strongly enough and continuously, i.e., the angular acceleration reads

$$\alpha_{\text{IRD}} = \frac{1}{J_z} \frac{dH1}{dt} \quad (1)$$

However, the 0-IPE interfaces (**Figure 2c**), which are nonsmooth, lead to intertube friction. That friction resists the rotation of the rotor, and the related angular deceleration of the rotor caused by the stator yields

$$\alpha_{\text{Stator}} = -\frac{1}{J_z} \frac{dH2}{dt} \quad (2)$$

where H2 is the angular momentum of the rotor about the *z*-axis, generated by the friction forces of atoms on the stator against the relative sliding of the rotor. The angular momentum H2 reads

$$H2 = \bar{r} \sum_{i=0}^{ns} F_i^t \quad (3)$$

where F_i^t is the tangent component of the friction force caused by the *i*th atom on the stator that has ns free atoms. The tangent direction is normal to the *z*-axis. \bar{r} is the average radius of the two tubes. J_z in **eqs 1** and **2** represents the mass moment of inertia of the rotor with respect to the *z*-axis and can be expressed as

$$J_z = \sum_{i=0}^{nr} m_i(x_i^2 + y_i^2) \quad (4)$$

where m_i is the *i*th atom at the point (x_i, y_i, z_i) of the rotor that has nr atoms. Hence, the rotational speed of the rotor can be obtained by integrating angular acceleration with respect to time:

$$\begin{aligned} \omega(t) &= \int_{s=0}^t (\alpha_{\text{IRD}} + \alpha_{\text{Stator}}) ds = \int_{s=0}^t \frac{1}{J_z} \frac{d(H1 - H2)}{ds} ds \\ &= \int_{H(s=0)}^{H(s=t)} \frac{1}{J_z} d(H1 - H2) \end{aligned} \quad (5)$$

Because the values of \bar{r} and F_i^t depend on the interaction between the rotor and the stator,¹⁷ the final stable rotational speed of the rotor is sensitive to temperature.

2.2. Methods. To explore the sensitivity of the dynamic behavior to temperature, we conduct a series of numerical tests for the nanomotor shown in **Figure 1**. Each numerical test uses the following eight steps:

- (1) Build the geometric model of the system as shown in **Figure 1** with ideal bond lengths and bond angles.
- (2) Choose two atoms at each end of the stator and specify their IRD.
- (3) Fix the atoms in the blue area on the stator.
- (4) Minimize the potential energy of the system. The convergence is controlled by the energy and force of atoms in the system (this step is optional).
- (5) Assign the initial velocity of the free atoms on the nanomotor by satisfying the given temperature of the system and obeying Gaussian distribution.
- (6) Place the system under a canonical *NVT* ensemble with the specified temperature. The tolerance of the temperature change from the specified temperature is set at 1%.
- (7) Run and record data for postprocessing.
- (8) Stop.

In simulating the rotation of the rotor shown in **Figure 1**, the AIREBO potential^{46,47} is used to describe the interaction among carbon and hydrogen atoms in the system. The potential energy contains the following three parts:

$$\left\{ \begin{array}{l} P = P_{\text{REBO}} + P_{\text{Torsion}} + P_{\text{L-J}} \\ P_{\text{REBO}} = \sum_i \sum_{j(j>i)} [V_{ij}^{\text{R}}(r_{ij}) - b_{ij} V_{ij}^{\text{A}}(r_{ij})] \\ P_{\text{Torsion}} = \frac{1}{2} \sum_i \sum_{j(j\neq i)} \sum_{k(k\neq i,j)} \sum_{l(l\neq i,j,k)} w_{ij}(r_{ij}) \cdot \\ \quad w_{jk}(r_{ij}) \cdot w_{kl}(r_{ij}) \cdot V_{\text{Torsion}}(\alpha_{ijkl}) \\ P_{\text{L-J}} = \sum_i \sum_{j(j>i)} 4\epsilon \left[\left(\frac{\sigma}{r_{ij}} \right)^{12} - \left(\frac{\sigma}{r_{ij}} \right)^6 \right] \end{array} \right. \quad (6)$$

where V_{ij}^{R} and V_{ij}^{A} in the short-range REBO potential P_{REBO} are repulsive and attractive pairwise potentials determined by the types of atoms *i* and *j*, respectively. r_{ij} represents the distance from atom *i* to atom *j*. b_{ij} indicates the many-body effect. P_{Torsion} depends on the dihedral angle (α_{ijkl}) from atoms *i*, *j*, *k*, and *l*. The positive bond weight w_{ij} is between 0 and 1. V_{Torsion} is the potential caused by the variation of α_{ijkl} . $P_{\text{L-J}}$ describes the nonbonded intermolecular interactions (Lennard-Jones interaction) with $\sigma_{\text{C-C}} = 0.34$ nm, $\sigma_{\text{H-H}} = 0.265$ nm, $\sigma_{\text{C-H}} = (\sigma_{\text{C-C}} + \sigma_{\text{H-H}})/2$, $\epsilon_{\text{C-C}} = 2.84$ meV, $\epsilon_{\text{H-H}} = 1.5$ meV, $\epsilon_{\text{C-H}} = 1.376$ meV. The cutoff equals $3\sigma_{\text{C-C}}$.

The time increment for integration of Newton's second law of motion is set at 0.001 ps. The Nosé–Hoover thermostat is adopted to modify the velocities of atoms in each simulation, which is carried out using open source code LAMMPS.⁴⁸ In controlling temperature, the kinetic energy of the rotor with

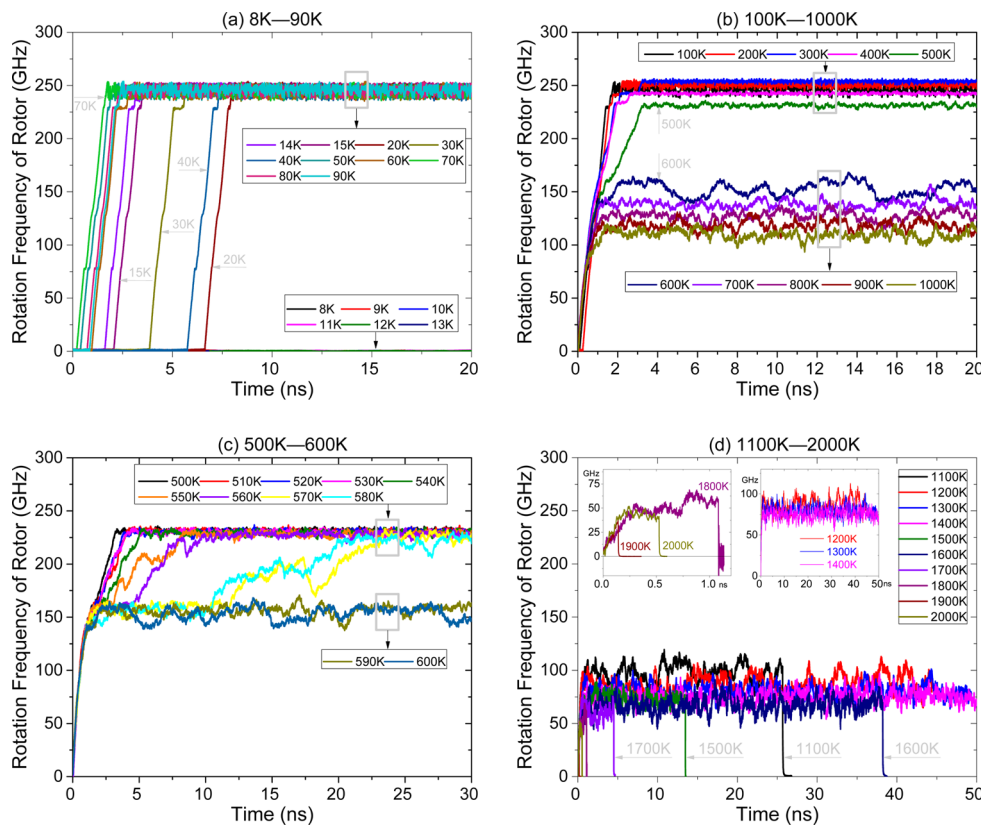


Figure 3. History curve of rotational frequency of the rotor (ω) in Figure 1 at different temperatures (T): (a) T is in [8, 90] K; (b) T is in [100, 1000] K; (c) T is in [500, 600] K; (d) T is in [1100, 2000] K.

respect to rigid motion, i.e., translation or rotation, is removed from the total kinetic energy of the system.

3. RESULTS AND DISCUSSION

3.1. Spectrum of Rotational Frequency of the Rotor versus System Temperature. In the solutions illustrated in Figure 3a, the rotor is barely excited to rotate within 20 ns when the temperature is below 14 K. Meantime, the stable values of rotational frequency of the rotor ω at the temperature interval [14, 90] K show very little difference, all values being close to 250 GHz. The values of ω have a slight fluctuation. These results demonstrate that the rotational frequency of the rotor at the given temperature interval is robust with respect to temperature. If we need a rotary nanomotor with a sensitive reaction of ω to temperature within 5 ns, i.e., such that the rotation of the rotor approaches a stable state within 5 ns, the temperature should be higher than 50 K. Commonly, the value of ω at higher temperatures requires less time to approach a stable state. But the sequence is not strictly monotonic. For example, the time needed to reach the stable value of ω at 70 K is shorter than that for ω at 90 K (in Figure 3a) or similarly ω at 100 K vs at 500 K in Figure 3b.

In Figure 3b, the values of ω within the temperature interval [100, 400] K are also robust with respect to temperature. The stable values of ω at 400 and 500 K are obviously different from those at \sim 10 GHz (about 10 GHz). But clearly, the difference is much less than the \sim 80 GHz difference between the values of ω at 500 and 600 K (Figure 3c). From 1100 to 2000 K (Figure 3d), the value of ω is much more sensitive to temperature. At the same time, after 5 ns the values of ω at a temperature within [600, 1700] K show considerable

fluctuation; i.e., the standard deviation of ω is much greater than that at [100, 400] K. Another phenomenon illustrated is that the value of ω at $T \geq 1100$ K drops suddenly to zero after a period of the rotor running. For example, ω at 1500 K becomes zero after \sim 14 ns (about 14 ns), whereas at 1700 K the drop occurs before the rotor has achieved 5 ns of rotation. As we observe from the curves in Figure 3d, ω finally becomes zero when T is no less than 1500 K. From the curve of ω at 1100 K, we may predict that the values of ω at 1200, 1300, and 1400 K could also become zero after a long period of time.

From the above discussion, the following four questions should be answered to understand the relationship between the stable value of ω and temperature:

3.1.a. Why Does ω at Higher Temperatures Need Less Time To Approach a Stable Value? From Figure 3a, we find that the sharp increase of ω at 15 K occurs near 2 ns (Movie 1 in Supporting Information). The value of ω at 70 K jumps up after no more than 0.5 ns of running. The difference is actually caused by the collision between the rotor and atoms with IRD on the stator at different temperatures (Figure 2). For example, at a lower temperature, the amplitude of oscillation of atoms on the rotor is smaller. Hence, collisions between the rotor and atoms with IRD provide less angular momentum, an effect that is significant for the angular acceleration of the rotor (see H1 in eq 1). Moreover, at the lower temperature, the likelihood of collision between the rotor and atoms with IRD must be lower than that at higher temperatures. At the same time, the friction force between the two tubes is static friction. Only when the collision provides higher angular momentum than the friction force, i.e., $H_1 > H_2$ (in eq 4), can the rotation of the rotor be actuated. Therefore, at higher temperatures, the rotor can be

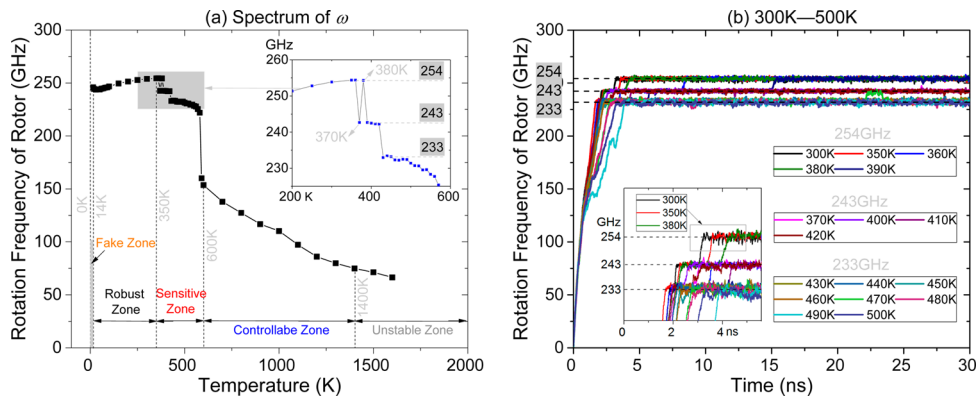


Figure 4. Curves of ω : (a) curve of the stable value of ω vs temperature within [14, 1600] K in Figure 3; (b) history curves of rotational frequency of the rotor at T in [300, 500] K.

Table 1. Spectrum of ω of the Rotor at Temperatures within [15, 1800] K^a

| temperature (K) | | | | | | | | | | |
|-----------------|-------|-------|--------|-------|-------|-------|--------|--------|-------|-------|
| ω (GHz) | 15 | 20 | 30 | 40 | 50 | 60 | 70 | 80 | 90 | 100 |
| 245.9 | 244.4 | 243.7 | 244.0 | 243.9 | 244.6 | 244.9 | 245.5 | 245.8 | 246.7 | |
| temperature (K) | | | | | | | | | | |
| 200 | 300 | 350 | 360 | 370 | 380 | 390 | 400 | 410 | 420 | |
| ω (GHz) | 251.4 | 253.9 | 254.4 | 242.6 | 242.7 | 254.3 | 242.7 | 242.5 | 242.3 | 242.2 |
| temperature (K) | | | | | | | | | | |
| 430 | 440 | 450 | 460 | 470 | 480 | 490 | 500 | 510 | 520 | |
| ω (GHz) | 233.0 | 233.4 | 233.2 | 232.3 | 232.2 | 232.5 | 232.4 | 231.4 | 230.7 | 230.6 |
| temperature (K) | | | | | | | | | | |
| 530 | 540 | 550 | 560 | 570 | 580 | 590 | 600 | 700 | 800 | |
| ω (GHz) | 229.5 | 229.6 | 228.3 | 227.7 | 225.4 | 221.9 | 160.1 | 153.6 | 137.9 | 127.4 |
| temperature (K) | | | | | | | | | | |
| 900 | 1000 | 1100 | 1200 | 1300 | 1400 | 1500 | 1600 | 1700 | 1800 | |
| ω (GHz) | 116.8 | 110.2 | 97.2 × | 86.1 | 79.8 | 74.9 | 71.3 × | 66.4 × | × | × |

^aLabel “×” represents a sudden stoppage.

actuated to rotate more quickly. This conclusion can be verified easily from the curves in Figure 3b.

3.1.b. Why Does the Stable Value of ω Increase from 243.9 GHz at 50 K to 253.9 GHz at 300 K and Subsequently Decrease Continuously? From the curves in Figure 4a and Table 1, we know that the rotational frequency (ω) reaches its maximum at 350 K. This finding indicates that the value of ω increases with an increase in temperature up to 350 K. The mechanism is that the dramatic collisions between the rotor and atoms with IRD significantly increase the friction between the two tubes. When T is greater than 350 K, the dynamic friction between the two tubes increases more quickly and the duration of acceleration of the rotor is reduced. Hence, the final stable value of ω becomes smaller than that at 350 K. As the temperature increases, the friction increases more quickly due to the stronger interaction between two tubes with the high amplitude of vibration of the atoms. Hence, the rotational frequency of the rotor decreases after the temperature exceeds 350 K. This conclusion seems different from the results in our previous work.³⁹ The reason is that the present stator has a large number of free atoms that provide a major contribution to the friction between the two tubes, because the free atoms on the stator can have inward displacement that increases the normal compression between the two tubes and further leads to higher friction. In either model, stable rotational frequency of

the rotor (eq 5) is reached only when H1 is no longer greater than H2.

We also find that the value of ω drops monotonically from 600 to 1600 K if we do not consider the sudden stoppage of the rotor. From the foregoing discussion and considering the curve shown in Figure 4a, we divide the temperature interval [14, 2000] K into five zones for the present model, namely, a fake zone (FZ) when T is in [0, 14] K, a robust zone (RZ) when T varies from 14 to 350 K, a sensitive zone (SZ) with T in [350, 600] K, a controllable zone (CZ) with T in [600, 1400] K, and an unstable zone (UZ) when T exceeds 1400 K. Here we set 1400 K rather than 1100 K as the boundary of CZ and UZ because the stable rotation of the rotor is maintained for ~25 ns. In the design of a thermally driven rotary nanomotor, the zones should be estimated first. For example, when we need to design a nanomotor with varying rotational frequency of the rotor, we should first find the temperature field with respect to the CZ. If we need a thermally driven nanomotor with stable rotational frequency of the rotor, the temperature interval with respect to the RZ should be estimated.

3.1.c. What Causes the Sharp Jumps of ω of the Rotor at T between 300 and 500 K? In the SZ, another phenomenon is found: there are only three distinct values of ω when T is within [300, 500] K. The three values are ~233 GHz, ~243 GHz, and ~254 GHz (see Figure 4b). For example, the

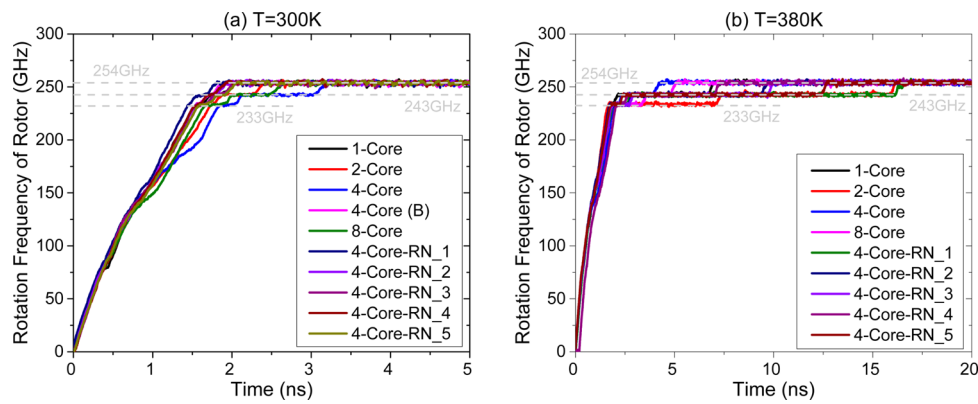


Figure 5. Tests of the effect of a random number (RN) of cores used in parallel computing on the final rotational frequency of the rotor. Most of the curves have three steps, at 233, 243, and 254 GHz levels. (a) $T = 300\text{ K}$. Within 3.5 ns, all the curves of ω are aligned at the 254 GHz level. “(B)” represents another computer. (b) $T = 380\text{ K}$. Within 17.5 ns, all the values converge to $\sim 254\text{ GHz}$. In particular, using a 1-Core computer, ω arrives at $\sim 254\text{ GHz}$ within 7 ns. The RN and core number influence the length of steps rather than the final stable value of ω . Hence, the values in Figure 4a (or Table 1) are acceptable.

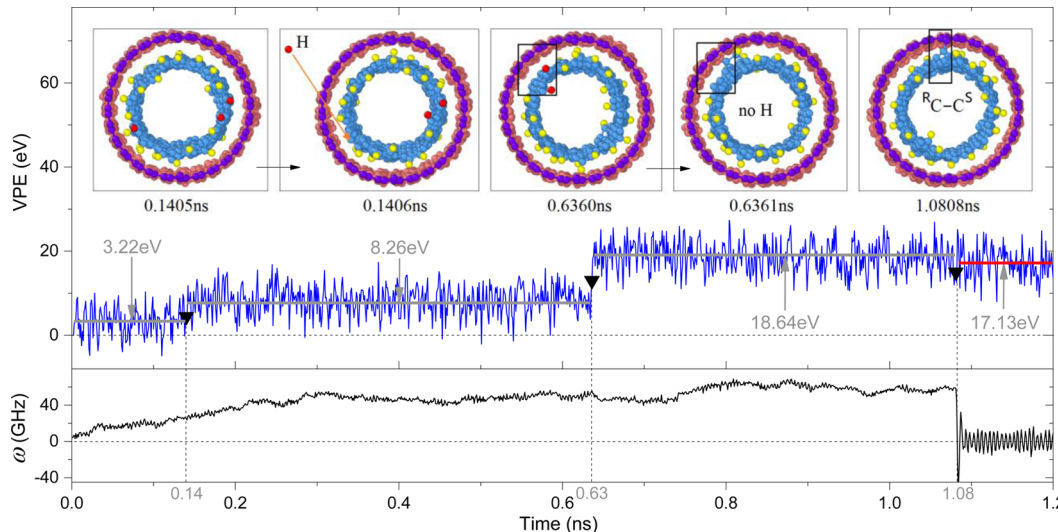


Figure 6. Some snapshots of the nanomotor running at 1800 K. At 0.1406 ns, a dark gray hydrogen atom escapes from the rotor (Movie 2). The value of the VPE of the system increases by $\sim 5\text{ eV}$. Two other dark gray hydrogen atoms disappear at 0.6361 ns (Movie 3). The value of the VPE increases by $\sim 10.3\text{ eV}$. At 1.0808 ns, an unsaturated carbon atom on the rotor (${}^{\text{R}}\text{C}$) is bonded with a carbon atom (C^{S}) with an IRD atom on the stator (Movie 4). The VPE value decreases by $\sim 1.5\text{ eV}$. Hence, the rotational frequency drops suddenly.

rotational frequency of the rotor experiences two or three of the step values when $T \leq 320\text{ K}$. In particular, when $T = 300, 350$, and 380 K , the curves of ω jump from $\sim 233\text{ GHz}$ to $\sim 243\text{ GHz}$ and finally to $\sim 254\text{ GHz}$ within 2 ns. It can also be verified that the jumps are sensitive to the RN that is adopted to specify the initial distribution of velocities of atoms in the system at a given temperature (e.g., step 5 in section 2). But the final stable value of ω is independent of the RN of atoms (Figure 5) and can be reached within 20 ns. From eq 5, it can be explained that the acceleration of ω caused by collisions with atoms with IRD and the deceleration of ω caused by friction between the two tubes are very sensitive to the initial state of the system, e.g., the distribution of the initial velocities of atoms on tubes. That means that at each step, the rotor is in a very weak equilibrium state during rotation at the current velocity. Mathematically, the potential energy of the system is a function of the positions of atoms (eq 6). Near the current configuration of the system, more than one local minimum of potential function exists (e.g., see the white-blue interfaces in Figure 2c). In calculation of the linear acceleration of the atoms, the result

of variation of potential energy (VPE) with respect to the positions of atoms approaches one of the local extrema. The values of linear acceleration of each atom are slightly different at different extreme points. That slight difference still affects the velocities of the atoms, those velocities being modified by the Nosé–Hoover thermostat. Further, the weak equilibrium state of the system may be changed by that effect, which finally leads to the sharp jump in the rotational frequency of the rotor. The phenomenon is very common in thermally driven nanomotor systems (see Figure 3). Hence, to obtain the most stable state of the rotor, the simulation time should not exceed 10 ns using single-core computation. In the SZ shown in Figure 4a, the value of ω becomes more sensitive to the temperature of the system when T is between 580 K ($\omega \approx 221.9\text{ GHz}$) and 590 K ($\omega \approx 160.1\text{ GHz}$). This sensitivity just indicates the steeper gradient of ω with respect to temperature. Hence, this sensitivity is different from the step-valued sensitivity of rotation of the rotor at 300 K .

3.1.d. Why Does the Rotor Stop Suddenly at Very High Temperature? By checking the configurations of the rotor at a

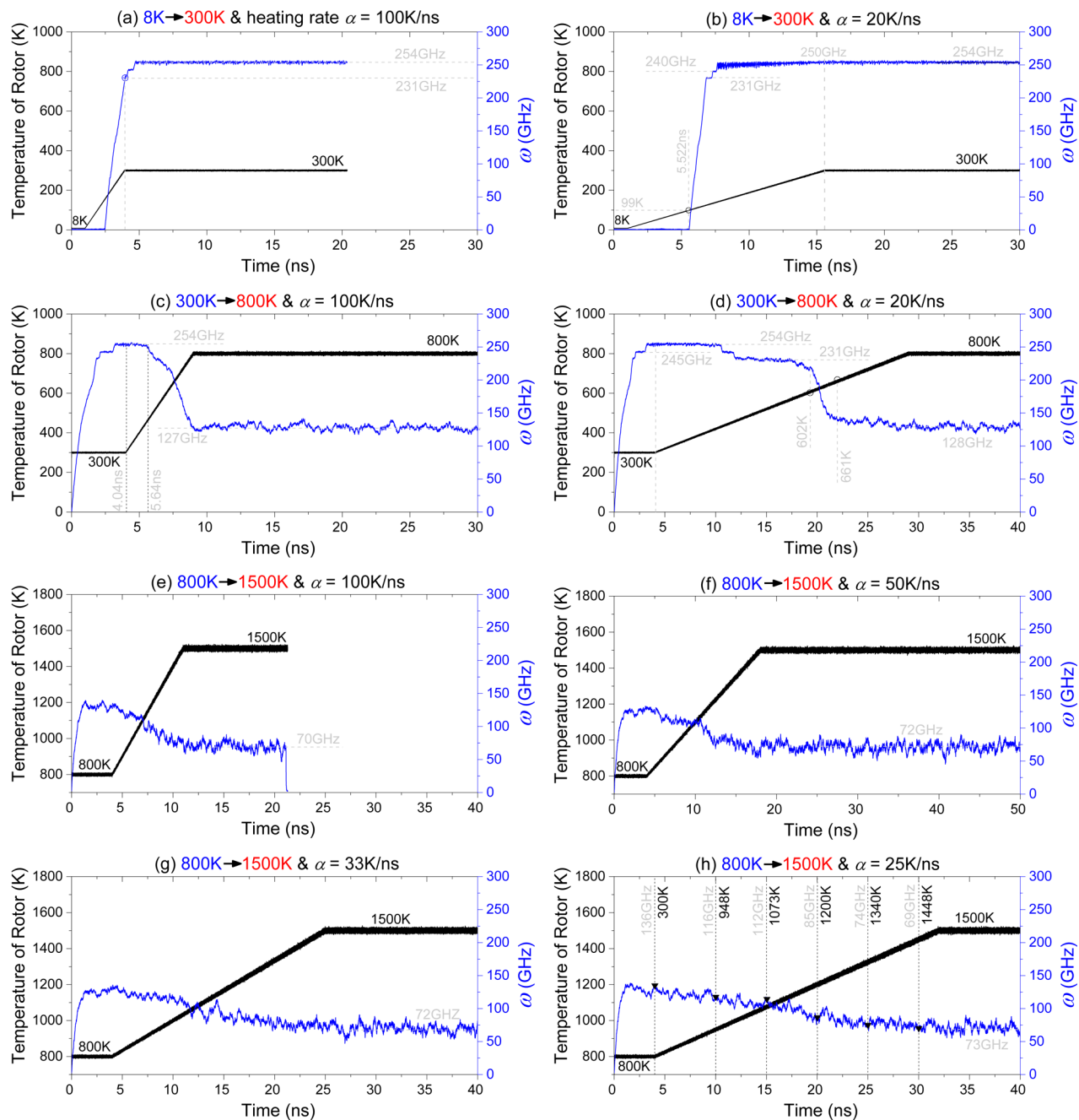


Figure 7. Response of rotation of rotor during heating from ultralow temperature (8 K) to high temperature (1500 K) at different heating rates.

high temperature, say 1800 K, we discovered that the hydrogen atoms on the rotor disappeared soon after the simulation began. At 0.1406 ns, for instance, a hydrogen atom (Figure 6), labeled in dark gray at 0.1405 ns, moves away from the rotor. This phenomenon is known as dehydrogenation, and Yu and Liu⁴⁹ reported that the critical temperature of dehydrogenation was around 1800 K. Dehydrogenation can also be revealed from variation of the potential energy (VPE) of the system, i.e., the difference between the system's current and initial potential energy. Due to the breakage of C–H bonds on the rotor, the VPE of the system clearly increases.

On the other hand, from the curve of the rotational frequency of the rotor, it can be found that the value of ω approaches a peak after 0.8 ns. However, due to marked vibration of the atoms on the rotor with unsaturated carbon

atoms at the ends, a new C–C covalent bond is generated between the rotor and stator. The VPE drops \sim 1.5 eV as the new C–C bond appears. That strong C–C bond forces the rotation of the rotor to stop.⁵⁰ Hence, at high temperature, the system is unstable and also the rotation of the rotor cannot be maintained.

3.2. Rotational Frequency of Rotor at Varying Temperature. Most previously reported numerical tests have focused on the dynamic response of nanomotors at a constant temperature. The results have implied that the rotational frequency or the dynamic behavior of the rotor is dependent on temperature. In practice, the temperature can vary over a relatively wide range. Then, the stability of the five zones of temperature with respect to the rotation of the rotor must be investigated. For example, the robustness of rotation

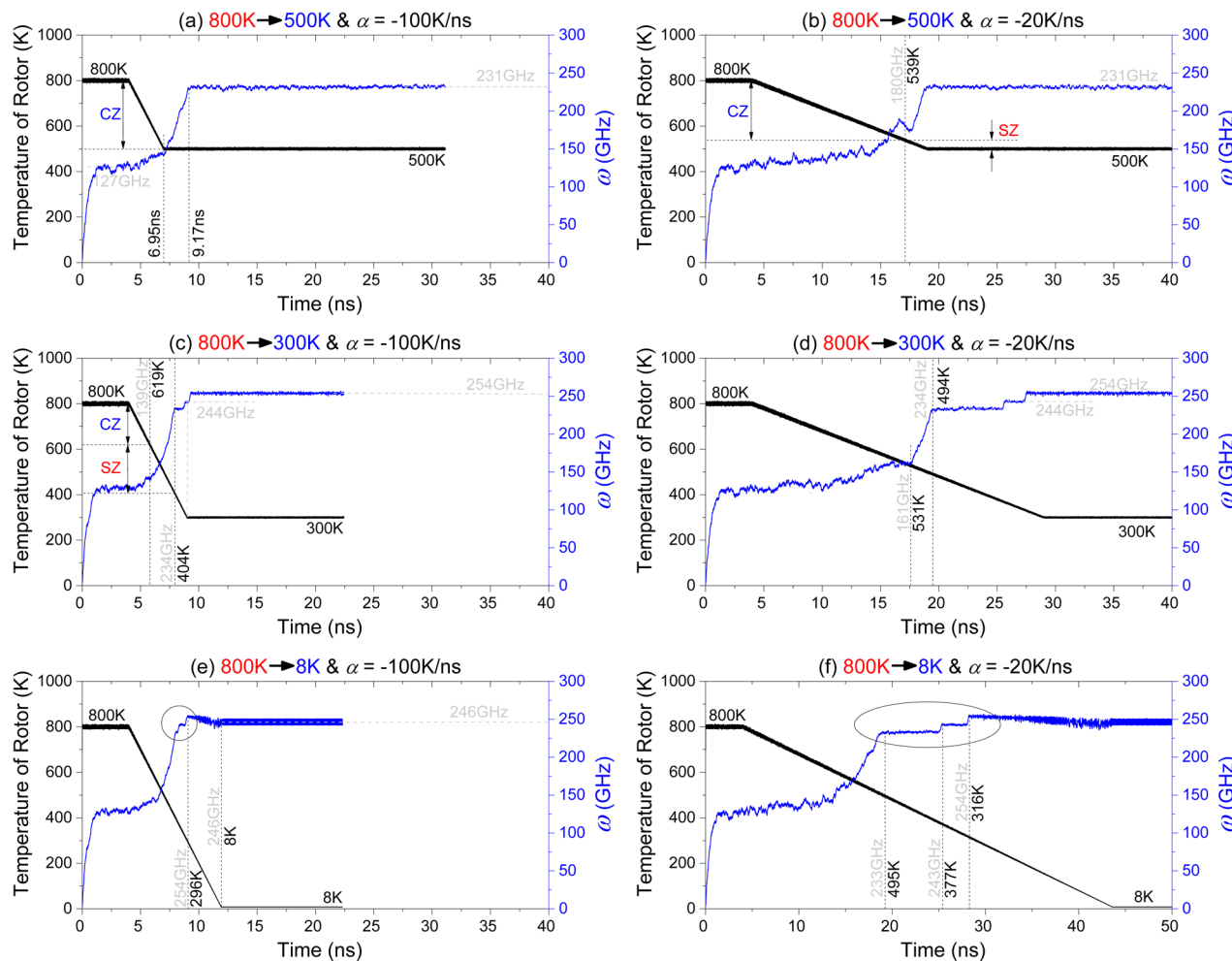


Figure 8. Response of rotation of rotor in cooling processes from 800 to 8 K at different heating rates.

can still be found in the RZ of temperature when a constant rotational frequency of the rotor is required. On the other hand, the rotational frequency can be adjusted to the required value by changing the temperature in the CZ. In this section, both heating and cooling processes of the rotor are considered, to reveal the rotation response.

3.2.a. Heating Process. In Figure 7, the effects of heating rate on the final stable rotation of the rotor are illustrated. When T increases from 8 to 300 K, the rotational frequency increases from zero to the final stable value of ω , which is independent of the heating rate, as evidenced by the observation that ω approaches ~ 254 GHz at either $\alpha = 100$ or 20 K/ns. The difference between the curves in Figure 7a and Figure 7b has two features of note. One is that the transient rotational frequency of the rotor at 300 K is ~ 231 GHz at the higher heating rate but ~ 250 GHz at the lower heating rate. The other is that the length of the RZ (Figure 4a) of temperature is much greater at a lower heating rate. Meanwhile, at $\alpha = 20$ K/ns, ω experiences a sharp jump from zero to ~ 231 GHz at 99 K, which is much higher than 15 K (Figure 3a). The reason is that the angular momentum on the rotor during collision with atoms with IRD needs to accumulate before the temperature approaches 99 K (eq 5), i.e., the coordinate state (a dynamic balance state) of the nanomotor approaches when the temperature of the system reaches 99 K.

When the temperature increases from 300 to 800 K (Figure 7c and Figure 7d), consistent with the foregoing discussion, the

frequency of the rotor experiences three zones (Figure 4a), i.e., RZ, SZ, and CZ, one after another. Therefore, the curve of ω also shows a related variation from accelerating rotation to stable rotation, then to deceleration rotation, and finally to stable rotation of the rotor at 800 K. During [0, 4] ns, the rotation of the rotor increases from zero to the stable state with ~ 254 GHz (which is the same as that at 300 K). During the heating process with $\alpha = 100$ K/ns (Figure 7c), ω retains a stable value for only ~ 1.6 ns and then drops to ~ 127 GHz. If the heating rate is only 20 K/ns (Figure 7d), we find that the SZ is reduced to [602, 661] K. The RZ, i.e., [300 K, 600] K, is wider than that given in Table 1 ([300, 540] K). We can predict that before approaching 602 K, if the temperature decreases slowly (e.g., with $\alpha = -20$ K/ns), the value of ω will increase again; i.e., it can be well controlled within [231, 254] GHz. Further related discussion is given below, separately.

If the temperature increases continuously from 800 to 1500 K, the curve of ω in Figure 7e-h shows the variation of ω with temperature. From Figure 3d, it can be seen that the rotation of the rotor is not always stable when T is 1100 K or greater. At 1500 K, the rotation of the rotor is stable for only ~ 14 ns and is followed by a sudden stoppage. When the rotor is heated with $\alpha = 100$ K/ns (Figure 7e), it does not stop suddenly during the heating process. After ~ 10 ns of constant temperature at 1500 K, the rotor stops suddenly. An interesting phenomenon appears when the rotor is heated at a lower heating rate, e.g., $\alpha = 50$ K/ns. In Figure 7f, the curve of ω retains a slight

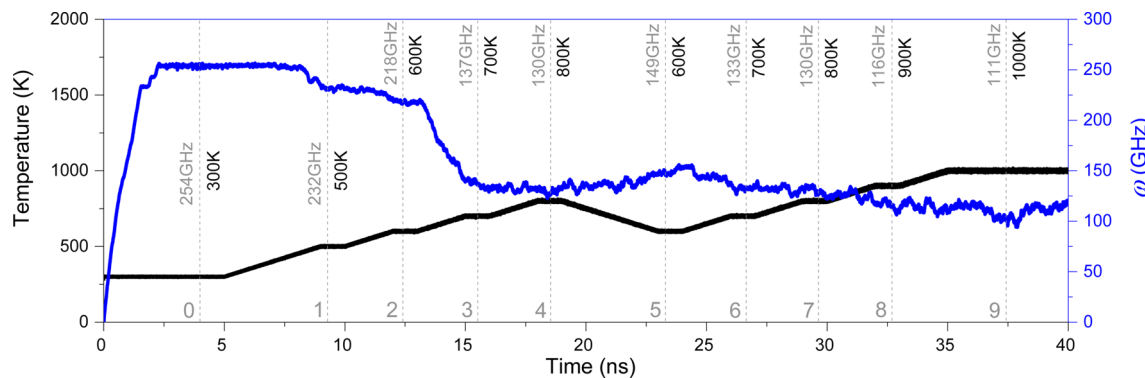


Figure 9. Response of rotation of rotor in alternating heating–cooling processes with different heating rates. The entire process encompasses nine heating or cooling stages. The heating and cooling ratios are 50 K/ns and -50 K/ns, respectively. When the temperature approaches an objective value, it remains unchanged for 1.0 ns. For example, during the increase from 300 to 500 K, the temperature remains unchanged at 500 K for 1 ns.

fluctuation at 1500 K and does not ever drop to zero because T arrives at 1500 K at 18 ns. The time averaged value of ω is ~ 72 GHz, which matches that of ω at 1500 K well (Table 1). This phenomenon also occurs at a lower heating rate, e.g., 33 or 25 K/ns. Hence, sudden stoppage of the rotor at 1500 K occurs with very low probability. This finding also indicates that dehydrogenation of the rotor does not occur at 1500 K. Moreover, the value of ω decreases continuously during the heating process, indicating that [800, 1500] K can also be considered a controllable zone.⁵¹

3.2.b. Cooling Process. Temperature adjustment can be achieved by both heating and cooling processes. Hence the rotational behavior of the rotor in the cooling process must be investigated. Here, the initial temperature is set at 800 K rather than 1500 K. Figure 8 gives the relevant numerical results.

In the cooling process with the temperature decreasing from 800 to 500 K at the rate of $\alpha = -100$ K/ns (see Figure 8a), the value of ω increases monotonically, indicating that the temperature interval [300, 800] K belongs to the CZ. In the subsequent ~ 2.2 ns at 500 K, the value of ω jumps sharply from ~ 150 GHz to ~ 231 GHz. This finding demonstrates that the width of the SZ is zero. Actually, this period can be considered an accumulation of ω (eq 5). When the negative heating rate is -20 K/ns (Figure 8b), the CZ spans from 539 to 800 K, and the narrow SZ increases from 500 K (with $\omega \approx 231$ GHz) to 539 K (with $\omega \approx 180$ GHz).

If the temperature decreases from 800 to 300 K continuously with $\alpha = -100$ K (Figure 8c), the CZ spans from 619 to 800 K. The width of the SZ starting from 404 to 619 K is much greater than that from 494 to 531 K with the lower heating rate of -20 K/ns (Figure 8d). Compared with the widths of the SZ in Figure 8a and Figure 8b, we find that a higher rate of temperature decrease with a higher rate of cooling leads to a wider SZ.

If the system is cooled from 800 to 8 K (at 8 K the rotor should have no rotation), an interesting phenomenon is observed. The rotational frequency of the rotor undergoes a rapid increase from ~ 127 GHz at 800 K to the peak value of ~ 254 GHz at 296 K when $\alpha = -100$ K/ns (Figure 8e). From 296 to 8 K, the value of ω shows only a slight drop from ~ 254 GHz to ~ 246 GHz rather than 0 GHz. This finding indicates that the rotor is rotating at an ultrahigh speed at 8 K. If the cooling rate is -20 K/ns (Figure 8f), ω approaches its peak value at 316 K. After that, the final stable value of ω is still ~ 246 GHz at 8 K. From the circled area in Figure 8e and Figure 8f, stepped values of ω occur during cooling. This finding indicates

that the RZ (in which the rotor rotates at a weak equilibrium state) becomes wider at a lower cooling rate. The same conclusion can also be obtained from Figure 8c and Figure 8d. In the period that covers the decrease of ω from its peak value (~ 254 GHz) to the stable value (~ 246 GHz), the angular momentum caused by intertube friction is slightly greater than that caused by collision between the rotor and IRD atoms. When the rotor is rotating at the 8 K, the intertube friction becomes negligible because the collisions between the rotor and the atoms with IRD provide very low impulses onto the rotor. Hence, it is possible to design a high-speed rotary nanomotor at an ultralow temperature.

3.2.c. Alternating Heating–Cooling Process. To show the response speed of the output rotation of the rotor with respect to the variation of temperature, we adopt an alternating heating–cooling process. The temperature begins to increase from 300 to 800 K, then decreases to 600 K, and then further increases to 1000 K. At certain specified values of temperature, e.g., 500 K, 600 K, 700 K, 800 K, 900 K, the heating or cooling ratio is zero for 1.0 ns. The curves shown in Figure 9 illustrate the variation histories of temperature and the related rotational frequency of the rotor. At each stage, the time averaged value of the rotational frequency of the rotor is labeled. It can be found that at 600 K during the heating process (stage 2), the mean value of ω is ~ 218 GHz, which is obviously greater than that at stage 5 (during the cooling process). The reason is that the temperature is at the edge of the SZ of temperature (Figure 4a). If the temperature is beyond the SZ, for example, $T = 700$ or 800 K, the rotational frequency of the rotor differs slightly during different heating processes. This finding verifies that the value of the rotational frequency of the rotor at the temperature at the CZ (Figure 4a) is controllable with high sensitivity. Moreover, at other temperatures in the CZ, e.g., 900 or 1000 K, the value of the rotational frequency of the rotor also matches that of the rotor at the constant temperature (Table 1). Hence, the curve of rotational frequency vs temperature is significant as a guideline for fabricating a temperature-controlled rotor with a specified rotational frequency.

4. CONCLUSION

To understand the mechanism of a thermally driven rotary nanomotor made from DWCNTs, both theoretical and numerical analyses were performed. Theoretically, due to the asymmetry of the interaction potential energy (IPE) field between the rotor and stator with inward radial deviation (IRD) atoms, collisions between the rotor and atoms with IRD

drive the rotation of the rotor, and the roughness the interface of IPE isoline with respect to 0 eV resists the rotation. On the basis of the numerical results, some conclusions are drawn. First, the rotor reaches its maximal rotational frequency in the equilibrium state. Second, according to the spectrum of ω with respect to temperature from 8 to 2000 K, the temperature interval [8, 2000] K is divided into five zones, a fake zone, a robust zone (RZ), a sensitive zone, a controllable zone (CZ), and an unstable zone. Third, in the RZ, a nanomotor with a constant rotational frequency can be designed. Fourth, in the CZ in particular, the variable rotational frequency of the rotor can be adjusted by varying the temperature. Finally, if the rotating rotor is cooled from a higher temperature to an extremely low temperature at which the rotor cannot be actuated to rotate, the final stable value of the rotational frequency is slightly lower than the peak value, indicating that a high-speed rotary nanomotor can be designed according to this phenomenon.

■ ASSOCIATED CONTENT

S Supporting Information

The Supporting Information is available free of charge on the ACS Publications website at DOI: [10.1021/acs.jpcc.7b04734](https://doi.org/10.1021/acs.jpcc.7b04734).

- Movie 1 at 15 K during [1950, 2150] ps ([AVI](#))
- Movie 2 at 1800 K during [130, 150] ps ([AVI](#))
- Movie 3 at 1800 K during [625, 645] ps ([AVI](#))
- Movie 4 at 1800 K during [1070, 1090] ps ([AVI](#))

■ AUTHOR INFORMATION

Corresponding Authors

*E-mail: kuncai2008@163.com.

*E-mail: Qinghua.qin@anu.edu.au. Phone: +61 2 61258274.

ORCID

Qing H. Qin: [0000-0003-0948-784X](https://orcid.org/0000-0003-0948-784X)

Author Contributions

Author K.C. proposed the project, prepared part of the data. Authors J.Y. and J.S. built models and prepared part of the data. Authors K.C. and Q.H.Q. wrote the paper. All authors participated in writing and discussions.

Notes

The authors declare no competing financial interest.

■ REFERENCES

- (1) The Nobel Prize in Chemistry 2016. https://www.nobelprize.org/nobel_prizes/chemistry/laureates/2016/ (accessed June 15, 2017).
- (2) Wu, Z. G.; Wu, Y. J.; He, W. P.; Lin, X. K.; Sun, J. M.; He, Q. Self-Propelled Polymer-Based Multilayer Nanorockets for Transportation and Drug Release. *Angew. Chem., Int. Ed.* **2013**, *52*, 7000–7003.
- (3) Schamel, D.; Mark, A. G.; Gibbs, J. G.; Miksch, C.; Morozov, K. I.; Leshansky, A. M.; Fischer, P. Nanopropellers and Their Actuation in Complex Viscoelastic Media. *ACS Nano* **2014**, *8*, 8794–8801.
- (4) Baraban, L.; Streubel, R.; Makarov, D.; Han, L. Y.; Karnaushenko, D.; Schmidt, O. G.; Cuniberti, G. Fuel-Free Locomotion of Janus Motors: Magnetically Induced Thermophoresis. *ACS Nano* **2013**, *7*, 1360–1367.
- (5) Eelkema, R.; Pollard, M. M.; Vicario, J.; Katsonis, N.; Ramon, B. S.; Bastiaansen, C. W. M.; Broer, D. J.; Feringa, B. L. Nanomotor Rotates Microscale Objects. *Nature* **2006**, *440*, 163–163.
- (6) Magdanz, V.; Sanchez, S.; Schmidt, O. G. Development of a Sperm-Flagella Driven Micro-Bio-Robot. *Adv. Mater.* **2013**, *25*, 6581–6588.
- (7) Iijima, S. Helical Microtubules of Graphitic Carbon. *Nature* **1991**, *354*, 56–58.
- (8) Kroto, H. W.; Heath, J. R.; O'Brien, S. C.; Curl, R. F.; Smalley, R. E. C₆₀: Buckminsterfullerene. *Nature* **1985**, *318*, 162–163.
- (9) Cai, K.; Wan, J.; Wei, N.; Cai, H.; Qin, Q. H. Thermal Stability of a Free Nanotube from Single-Layer Black Phosphorus. *Nanotechnology* **2016**, *27*, 235703.
- (10) Novoselov, K. S.; Geim, A. K.; Morozov, S. V.; Jiang, D.; Zhang, Y.; Dubonos, S. V.; Grigorieva, I. V.; Firsov, A. A. Electric Field Effect in Atomically Thin Carbon Films. *Science* **2004**, *306*, 666–669.
- (11) Qin, Z.; Qin, Q.-H.; Feng, X. Q. Mechanical Property of Carbon Nanotubes with Intramolecular Junctions: Molecular Dynamics Simulations. *Phys. Lett. A* **2008**, *372*, 6661–6666.
- (12) Chen, N.; Lusk, M. T.; van Duin, A. C. T.; Goddard, W. A. Mechanical Properties of Connected Carbon Nanorings Via Molecular Dynamics Simulation. *Phys. Rev. B: Condens. Matter Mater. Phys.* **2005**, *72*, 085416.
- (13) Bichoutskaia, E.; Heggie, M. I.; Popov, A. M.; Lozovik, Y. E. Interwall Interaction and Elastic Properties of Carbon Nanotubes. *Phys. Rev. B: Condens. Matter Mater. Phys.* **2006**, *73*, 045435.
- (14) Zhang, H.; Cai, K.; Wang, L. Deformation of Single-Walled Carbon Nanotubes under Large Axial Strains. *Mater. Lett.* **2008**, *62*, 3940–3943.
- (15) Ozden, S.; Autreto, P. A.; Tiwary, C. S.; Khatiwada, S.; Machado, L.; Galvao, D. S.; Vajtai, R.; Barrera, E. V.; Ajayan, P. M. Unzipping Carbon Nanotubes at High Impact. *Nano Lett.* **2014**, *14*, 4131–4137.
- (16) Cumings, J.; Zettl, A. Low-Friction Nanoscale Linear Bearing Realized from Multiwall Carbon Nanotubes. *Science* **2000**, *289*, 602–604.
- (17) Guo, W. L.; Zhong, W. Y.; Dai, Y. T.; Li, S. A. Coupled Defect-Size Effects on Interlayer Friction in Multiwalled Carbon Nanotubes. *Phys. Rev. B: Condens. Matter Mater. Phys.* **2005**, *72*, 075409.
- (18) Cook, E. H.; Buehler, M. J.; Spakovszky, Z. S. Mechanism of Friction in Rotating Carbon Nanotube Bearings. *J. Mech. Phys. Solids* **2013**, *61*, 652–673.
- (19) Zhang, R.; Ning, Z.; Zhang, Y.; Zheng, Q.; Chen, Q.; Xie, H.; Zhang, Q.; Qian, W.; Wei, F. Superlubricity in Centimetres-Long Double-Walled Carbon Nanotubes under Ambient Conditions. *Nat. Nanotechnol.* **2013**, *8*, 912–916.
- (20) Zheng, Q.; Jiang, Q. Multiwalled Carbon Nanotubes as Gigahertz Oscillators. *Phys. Rev. Lett.* **2002**, *88*, 045503.
- (21) Legolas, S.; Coluci, V.; Braga, S.; Coura, P.; Dantas, S.; Galvao, D. Molecular-Dynamics Simulations of Carbon Nanotubes as Gigahertz Oscillators. *Phys. Rev. Lett.* **2003**, *90*, 055504.
- (22) Guo, W.; Guo, Y.; Gao, H.; Zheng, Q.; Zhong, W. Energy Dissipation in Gigahertz Oscillators from Multiwalled Carbon Nanotubes. *Phys. Rev. Lett.* **2003**, *91*, 125501.
- (23) Cai, K.; Yin, H.; Qin, Q. H.; Li, Y. Self-Excited Oscillation of Rotating Double-Walled Carbon Nanotubes. *Nano Lett.* **2014**, *14*, 2558–2562.
- (24) Zhu, B. E.; Pan, Z. Y.; Wang, Y. X.; Xiao, Y. Thermal Effect on Dwcnts as Rotational Bearings. *Nanotechnology* **2008**, *19*, 495708.
- (25) Cai, K.; Cai, H.; Shi, J.; Qin, Q. H. A Nano Universal Joint Made from Curved Double-Walled Carbon Nanotubes. *Appl. Phys. Lett.* **2015**, *106*, 241907.
- (26) Cai, K.; Cai, H.; Ren, L.; Shi, J.; Qin, Q. H. Over-Speeding Rotational Transmission of a Carbon Nanotube-Based Bearing. *J. Phys. Chem. C* **2016**, *120*, 5797–5803.
- (27) Qiu, W.; Kang, Y. L.; Lei, Z. K.; Qin, Q. H.; Li, Q. A New Theoretical Model of a Carbon Nanotube Strain Sensor. *Chin. Phys. Lett.* **2009**, *26*, 080701.
- (28) Qiu, W.; Kang, Y. L.; Lei, Z. K.; Qin, Q. H.; Li, Q.; Wang, Q. Experimental Study of the Raman Strain Rosette Based on the Carbon Nanotube Strain Sensor. *J. Raman Spectrosc.* **2010**, *41*, 1216–1220.
- (29) Qiu, W.; Li, Q.; Lei, Z.-K.; Qin, Q.-H.; Deng, W.-L.; Kang, Y.-L. The Use of a Carbon Nanotube Sensor for Measuring Strain by Micro-Raman Spectroscopy. *Carbon* **2013**, *53*, 161–168.

- (30) Barreiro, A.; Rurali, R.; Hernandez, E. R.; Moser, J.; Pichler, T.; Forro, L.; Bachofen, A. Subnanometer Motion of Cargoes Driven by Thermal Gradients Along Carbon Nanotubes. *Science* **2008**, *320*, 775–778.
- (31) Zambrano, H. A.; Walther, J. H.; Jaffe, R. L. Thermally Driven Molecular Linear Motors: A Molecular Dynamics Study. *J. Chem. Phys.* **2009**, *131*, 241104.
- (32) Fennimore, A.; Yuzvinsky, T.; Han, W.-Q.; Fuhrer, M.; Cumings, J.; Zettl, A. Rotational Actuators Based on Carbon Nanotubes. *Nature* **2003**, *424*, 408–410.
- (33) Tu, Z.; Hu, X. Molecular Motor Constructed from a Double-Walled Carbon Nanotube Driven by Axially Varying Voltage. *Phys. Rev. B: Condens. Matter Mater. Phys.* **2005**, *72*, 033404.
- (34) Wang, B.; Vuković, L.; Král, P. Nanoscale Rotary Motors Driven by Electron Tunneling. *Phys. Rev. Lett.* **2008**, *101*, 186808.
- (35) Kang, J. W.; Hwang, H. J. Nanoscale Carbon Nanotube Motor Schematics and Simulations for Micro-Electro-Mechanical Machines. *Nanotechnology* **2004**, *15*, 1633–1638.
- (36) Hamdi, M.; Subramanian, A.; Dong, L.; Ferreira, A.; Nelson, B. J. Simulation of Rotary Motion Generated by Head-to-Head Carbon Nanotube Shuttles. *IEEE/ASME Transactions on Mechatronics* **2013**, *18*, 130–137.
- (37) Cai, K.; Li, Y.; Qin, Q. H.; Yin, H. Gradientless Temperature-Driven Rotating Motor from a Double-Walled Carbon Nanotube. *Nanotechnology* **2014**, *25*, 505701.
- (38) Rotating nanotube motors offer glimpse of future nanodevices. <https://phys.org/news/2014-12-rotating-nanotube-motors-glimpse-future.html> (accessed March 10, 2017).
- (39) Cai, K.; Wan, J.; Qin, Q. H.; Shi, J. Quantitative Control of a Rotary Carbon Nanotube Motor under Temperature Stimulus. *Nanotechnology* **2016**, *27*, 055706.
- (40) Cai, K.; Yu, J.; Wan, J.; Yin, H.; Shi, J.; Qin, Q. H. Configuration Jumps of Rotor in a Nanomotor from Carbon Nanostructures. *Carbon* **2016**, *101*, 168–176.
- (41) Cai, K.; Yu, J.; Liu, L.; Shi, J.; Qin, Q. H. Rotation Measurements of a Thermally Driven Rotary Nanomotor with a Spring Wing. *Phys. Chem. Chem. Phys.* **2016**, *18*, 22478–22486.
- (42) Yang, L.; Cai, K.; Shi, J.; Qin, Q. H. Significance Tests on the Output Power of a Thermally Driven Rotary Nanomotor. *Nanotechnology* **2017**, *28*, 215705.
- (43) Nosé, S. A Unified Formulation of the Constant Temperature Molecular Dynamics Methods. *J. Chem. Phys.* **1984**, *81*, 511–519.
- (44) Richard, C.; Robbins, H.; Stewart, I. *What Is Mathematics? An Elementary Approach to Ideas and Methods*; Oxford University Press: New York, 1996; p 344.
- (45) Hibbeler, R. C. *Engineering Mechanics: Dynamics*; Pearson Prentice Hall: Upper Saddle River, NJ, 2010; p 262.
- (46) Stuart, S. J.; Tutein, A. B.; Harrison, J. A. A Reactive Potential for Hydrocarbons with Intermolecular Interactions. *J. Chem. Phys.* **2000**, *112*, 6472–6486.
- (47) Li, S. Z.; Li, Q. Y.; Carpick, R. W.; Gumbsch, P.; Liu, X. Z.; Ding, X. D.; Sun, J.; Li, J. The Evolving Quality of Frictional Contact with Graphene. *Nature* **2016**, *539*, 541–546.
- (48) Plimpton, S. Fast Parallel Algorithms for Short-Range Molecular Dynamics. *J. Comput. Phys.* **1995**, *117*, 1–19.
- (49) Yu, D.; Liu, F. Synthesis of Carbon Nanotubes by Rolling up Patterned Graphene Nanoribbons Using Selective Atomic Adsorption. *Nano Lett.* **2007**, *7*, 3046–3050.
- (50) Cai, K.; Yu, J.; Yin, H.; Qin, Q. H. Sudden Stoppage of Rotor in a Thermally Driven Rotary Motor Made from Double-Walled Carbon Nanotubes. *Nanotechnology* **2015**, *26*, 095702.
- (51) Cai, K.; Yu, J. Z.; Shi, J.; Qin, Q. H. Robust Rotation of Rotor in a Thermal Driven Nanomotor. *Sci. Rep.* **2017**, *7*, 46159.